Supplementary Information

Understanding the role of facets and twin defects on the optical performance of GaAs nanowires for laser application

Zahra Azimi,[1] Nikita Gagrani,[1] Jiangtao Qu,[2] Olivier L. C. Lem,[3] Sudha Mokkapati,[4] Julie M. Cairney,[2] Rongkun Zheng,[5] Hark Hoe Tan,[1,6] Chennupati Jagadish,[1,6] Jennifer Wong-Leung[1]
[1]Department of Electronic Materials Engineering, Research School of Physics, The Australian National University, Canberra, ACT 2601, Australia.
[2]Aerospace, Mechanical and Mechatronic Engineering, The University of Sydney, Sydney, NSW 2006, Australia.
[3]Australian National Fabrication Facility ACT Node, Research School of Physics, The Australian National University, Canberra, ACT 2601, Australia.
[4]Department of Materials Science and Engineering, Faculty of Engineering, Monash University, Clayton, VIC 3800, Australia.
[5]The School of Physics, The University of Sydney, Sydney, NSW 2006, Australia.
[6] Australian Research Council Centre of Excellence for Transformative Meta-Optical Systems, Research School of Physics, The Australian National University, Canberra, ACT 2601, Australia.

Corresponding authors Email: zahra.azimi@anu.edu.au, jenny.wongleung@anu.edu.au

1. Growth and characterisation

1.1. Growth optimisation of GaAs nanowires

The substrates were prepared for nanowire (NW) growth using the following steps. First, a 30 nm-thick SiO_2 film was deposited on a GaAs (111)B wafer by plasma enhanced chemical vapor deposition. This was followed by spin coating an 80 nm-thick layer of ZEP-520A resist. The photoresist was then patterned with a Raith 150 electron beam lithography (EBL). The patterned resist consisted of 12 square arrays with a dimension of 200 µm × 200 µm, with holes of diameters ranging from 50 to 160 nm, and pitch sizes of 0.6 , 1 and 2 µm. The samples were then subjected to a 60 s chemical etching of the SiO_2 layer using a buffered HF solution. After chemical etching, the diameters of the holes increase, resulting in final hole diameters of 110 to 230 nm. ZEP-520A remover and oxygen plasma were then used to remove any residual resist within the holes.

GaAs NWs were grown on patterned substrates using an AIXTRON close-coupled showerhead reactor, at a pressure of 100 mbar. Trimethylgallium (TMGa) and AsH_3 were used as precursors of gallium and arsenic, respectively. The growth temperature and group V flow rate were optimized to achieve the highest nanowire aspect ratio (length/diameter) with good morphology. The morphology of the GaAs nanowires was characterized by an FEI-Verios 460 field emission scanning electron microscopy. For growth temperature optimisation, the flow rates of TMGa and AsH_3 were kept constant at 10^{-5} and 2×10^{-4} mol/min, respectively, corresponding to a V/III ratio of 20, while the growth temperature was varied between 720 to 795 ºC. All the samples were annealed for 10 min under an AsH_3 ambient prior to growth and the growth duration was 30 min. **Figure S1**a shows the variation in the aspect ratio (defined as length to diameter size) of GaAs NWs as a function of growth temperature for patterned substrates with a hole size of 190 nm and a pitch size of 1 µm. The highest aspect ratio of 28 was achieved for a growth

temperature of 765 ºC. In order to optimise the V/III ratio, the growth temperature and the TMGa flow rate were fixed at 765 ºC and 10^{-5} mol/min, respectively, and the AsH_3 flow rate was varied from 5×10^{-5} to 4×10^{-4} mol/min, corresponding to V/III ratios ranging from 5 to 40. At the lowest V/III ratio of 5, there was no NW growth. Figure S1b shows that the optimal V/III ratio of 20 yields the highest NWs length and aspect ratio. At an optimised growth temperature of 765 ˚C and a V/III (AsH_3/TMGa) ratio of 20, decreasing the growth time from 30 to 20 min decreased the NW length from 14 to 7 µm.

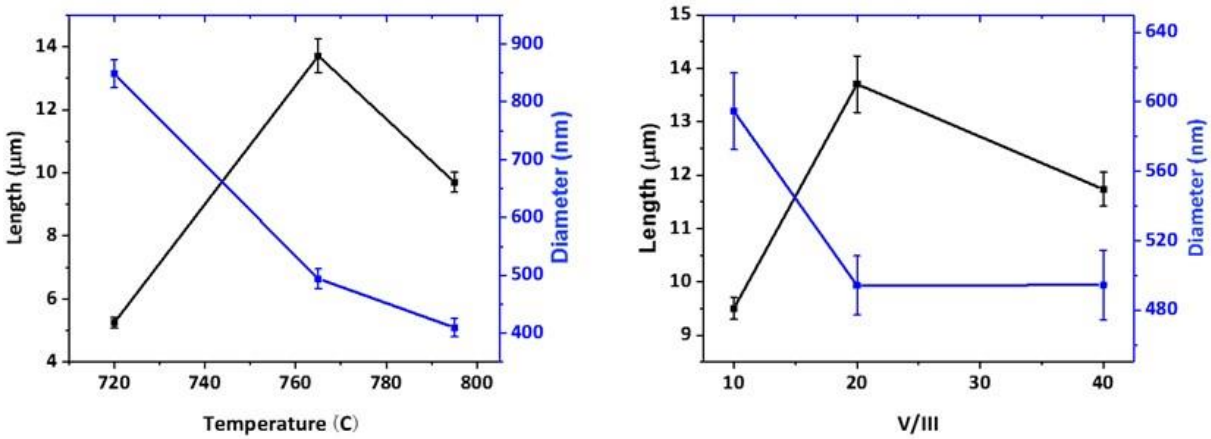

Figure S1. Nanowire length and diameter as a function of the (a) growth temperature at a constant V/III ratio of 20, and of the (b) V/III ratio at a constant growth temperature of 765 °C. Error bars represent the standard deviation over the nanowire array (the growth duration was 30 min).

1.2. Photoluminescence

Photoluminescence (PL) characterization was performed to assess the optical quality of the NWs as a function of the V/III ratio and growth temperature. In order to provide a quantitative assessment of the PL intensity, PL was carried out on nanowires with the same diameter of 500 nm for all growth conditions. These NWs were transferred onto SiO_2 substrates and measurements were carried out on single NWs using a 522 nm solid state pulsed laser, with a pump fluence of 15 µJ.cm^{-2} per pulse. The PL spectra were collected from the middle of the NWs. **Figure S2** shows that the nanowires grown with a V/III ratio of 20 at 765 ºC have the

highest PL intensity. As shown in **Figure S2**, the NWs grown with a V/III ratio of 20 at 765 ºC, had the highest aspect ratio and gave the highest PL intensity.

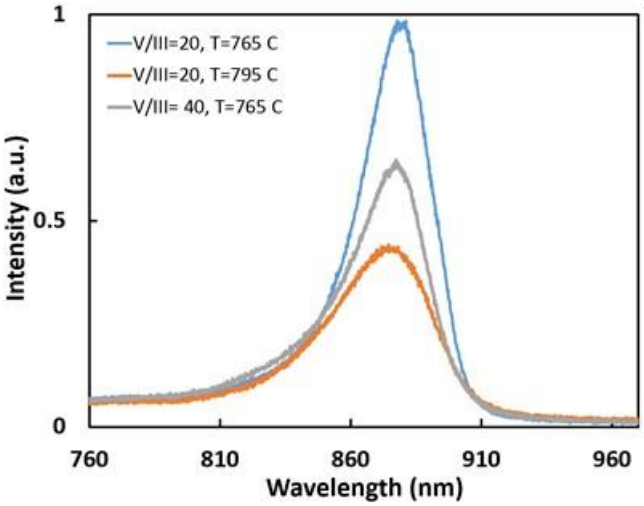

Figure S2. Room temperature PL measurements from single nanowires grown at different V/III ratios and temperatures.

1.3. Effect of hole diameter and pitch size

Figure S3 illustrates scanning electron microscopy (SEM) images of GaAs NW grown at the optimum temperature of 765 ºC and V/III ratio of 20 for 20 min. As shown, the GaAs nanowires are uniform in diameter and length for all hole diameters and pitch sizes except for a 2 µm region around the edge. The top view of the NWs shown in the insets for different hole diameters and pitch sizes confirms that all NWs have {110} side facets.

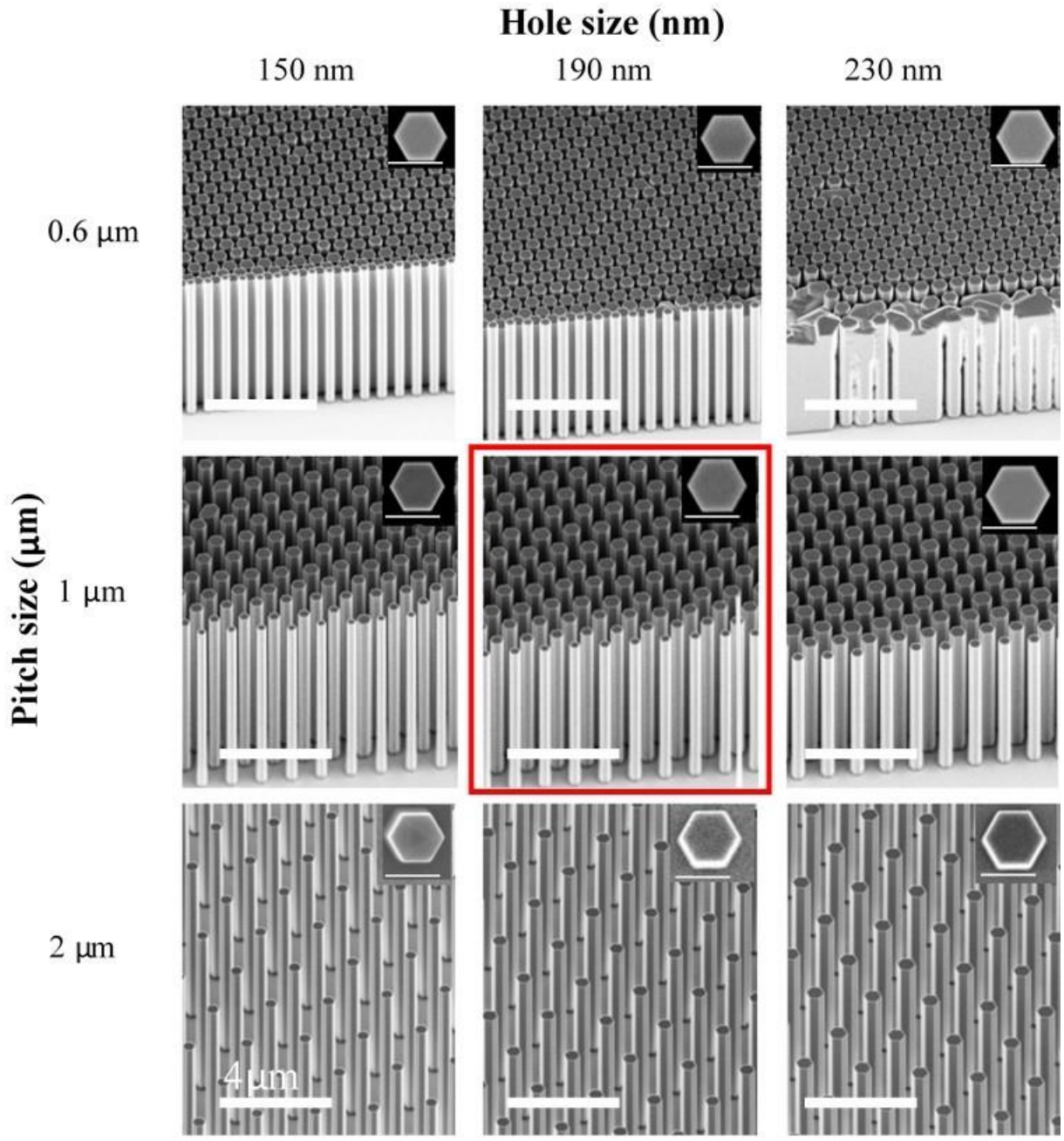

Figure S3. SEM images of GaAs nanowires, grown at 765 °C with a V/III ratio 20 for 20min with different hole and pitch sizes. Scale bar is 4 µm. Samples were viewed at a 45° tilt. Insets show the corresponding top view SEM images (scale bar is 0.5 µm). The NWs in the red frame were chosen to investigate optical characterization.

Increasing the pitch size from 0.6 to 2 µm increases both the NW diameter and length. Increasing the pattern hole size increases the NW diameter and decreases the NW length, while increasing the pitch size increases both the NW diameter and length, as shown in **Figure S4**.

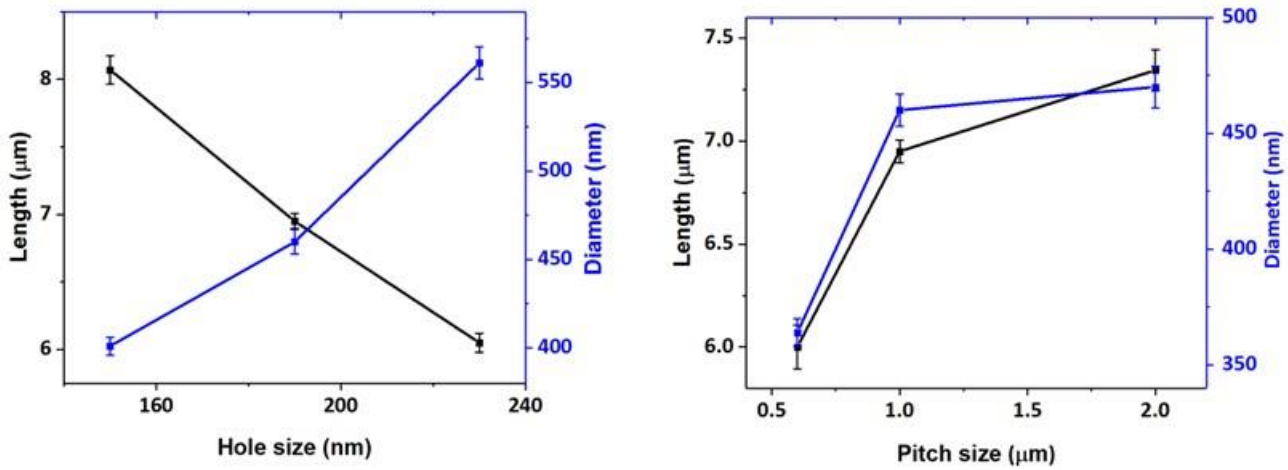

Figure S4. Nanowire length and diameter as a function of the (a) pattern hole sizes grown in a constant pitch size of 1 μm (b) pitch size in grown a constant hole size of 190 nm.

1.4. AlGaAs passivation

Another set of GaAs NW was passivated by depositing an AlGaAs shell around the GaAs core at the same temperature (765 °C) and the same the total group III flow rate (10^{-5} mol/min) for 45 seconds. Trimethylaluminium (TMAl) was used as the Al source and the ratio of TMGa/(TMAl + TMGa) and V/III (AsH_3/(TMGa + TMAl)) were 0.5 and 100, respectively. Finally, a layer of GaAs cap was grown for 1 min to prevent oxidation of the AlGaAs when exposed to atmosphere. The AlGaAs/GaAs shell/cap is measured to be 30±5 nm from SEM images of the nanowires with and without the AlGaAs shell/GaAs cap.

2. Identification of the nanowires base

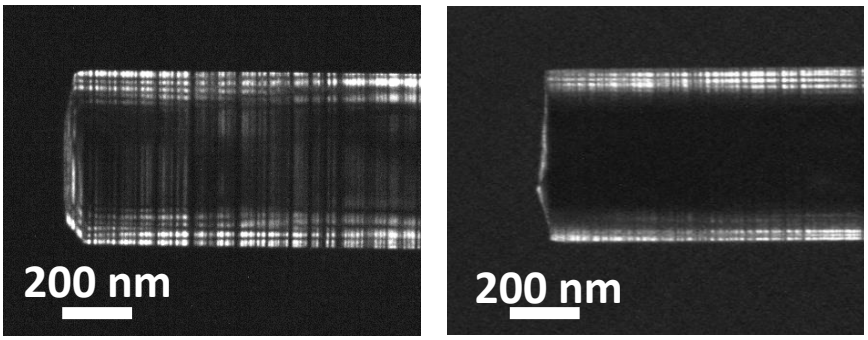

Figure S5. Dark-field TEM images of the cleaved facet at the nanowire base.

3. The effect of twin defects on optical properties

3.1. The effect of type II band alignment on CL emission

Because of their low formation energy, twin planes form easily in GaAs nanowires and their impact on the electronic band structure must be considered.[1–3] It has been proposed that the twin planes in a ZB nanowire structure can be considered as one repeat layer of WZ,[4] thereby creating a ZB/WZ/ZB heterostructure which has a type II band offset.[5,6] ZB GaAs has a direct band gap energy of 1.425 eV at room temperature.[7] However, the exact value of the band gap of WZ GaAs is still under dispute,[8,9] as well as the band offset at the ZB-WZ interface.[6,10–12] Despite ongoing efforts to provide further insights on the GaAs WZ electronic band structure, the formation of type-II band alignment at ZB-WZ interface is commonly accepted.

Previous studies have shown that the formation of WZ multilayers in a ZB structure resulted in a red shift of the PL emission peak.[5,11,13] Increasing the thickness of these WZ sections further red-shifted the emission peak.[11,13] In contrast, our structure has only unit layers of wurtzite (isolated twin defects), with decreasing density from the bottom to the top of the nanowire. To understand the mechanisms driving the observed red shift and the change of CL intensity[14], low temperature (80 K) CL was performed along the nanowire length.

Figure S6 shows low temperature (80 K) CL along the nanowire length. We could not identify CL emission peaks associated to impurities such as carbon at a temperature of 80 K. However, the latter temperature (the lowest possible with our setup) could be too high to detect very low amount of carbon impurities. The higher twin defects density toward the nanowire base do not give rise to new PL peaks. However, the red shift in the CL peak emission with increasing twin defect density toward the nanowire's base can be potentially ascribed to type II transitions.

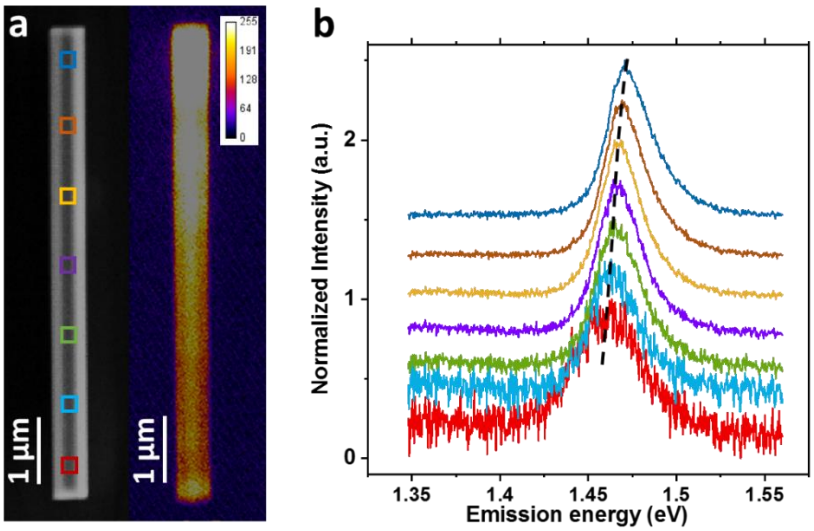

Figure S6. Low temperature (80 K) CL results from unpassivated GaAs nanowires. (a) SEM and CL intensities along a GaAs nanowire, and panchromatic CL image of the same nanowire. (b) CL spectra from the 7 colored boxes in (a).

3.2. Power- dependent PL spectra

At low temperature (8 K), non-radiative recombination pathways decrease enabling detection of emission from minor contributors such as type II emission peaks and impurities.[2,8,11,15] Figure S7 shows the PL spectra at 8 K of an unpassivated GaAs nanowire as a function of the excitation power collected from the middle of the nanowire.

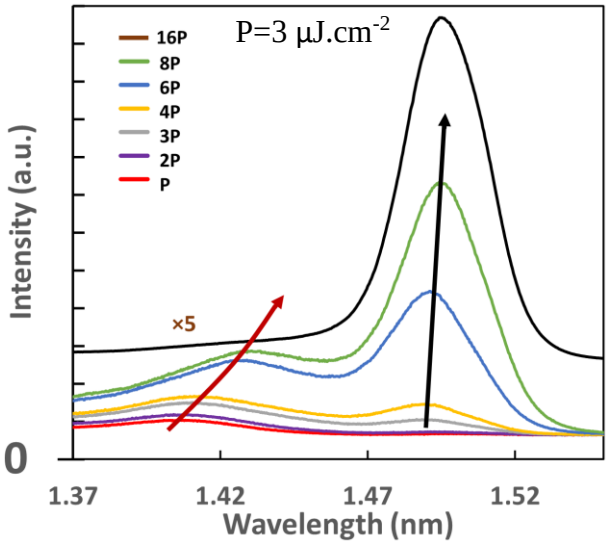

Figure S7. Power-dependent PL spectra at 8 K, collected from the middle of the unpassivated GaAs nanowires.

A 100×(NA=0.9) objective lens was used to excite the nanowires at different pump fluences. At a low excitation fluence of 3 μJ.cm^{-2} per pulse a single emission peak at 1.415 eV is observed. With increasing the excitation fluence to 9 μJ.cm^{-2} per pulse, another higher energy emission peak at 1.495 eV emerges, which could be attributed to free excitation recombination in ZB GaAs. This emission peak is lower than the reported free excitation recombination level[16] (1.515 eV) and might be related to the formation of twin-defects, composed of unit layer of WZ, in our nanowires. A similar red shift of the PL emission peak has also been reported by Senichev et al. for segments of GaAs nanowires having a twinned structure.[8]

By further increasing the excitation fluence to 24 μJ.cm^{-2} per pulse, the peak at 1.495 eV is blue-shifted by 7 meV, while the lower energy emission peak (1.415 eV) shows a larger blue-shift of about 22 meV. A higher excitation fluence of more than 30 μJ.cm^{-2} per pulse strongly increases the emission intensity from the free-recombination excitation (1.495 eV) peak at the expense of the lower energy emission peak, which is suppressed.

The presence of a lower energy emission peak between 1.44 and 1.49 eV at low temperature (less than 10 K) has been previously assigned to either the recombination of electron-hole pairs at ZB-WZ (type II band alignment)[15,17] or the presence of impurities.[1,3,4] With respect to the latter, spontaneous carbon doping of GaAs nanowires[17] has been attributed to the incomplete decomposition of TMGa,[18] and ascribed to a PL emission peak at 1.49 eV at low temperature.[17] However, our atomic probe tomography analysis reveals a highly pure GaAs composition with no detectable presence of carbon or other impurities (Figure S21 of the SI). Thus, we attribute the lower energy emission peak to the recombination of electron-holes at twin interfaces.

We also carried out a power-dependent PL measurement on our bare GaAs nanowire at room temperature. For this purpose, two spots located 1 μm away from the nanowires base and top were chosen as representative areas (Figure S8) with high (red circle) and low (blue circle) density of the twin defects, respectively.

At a low pump fluence of 5 μJ.cm^{-2} per pulse, we observed emissions at lower energy levels (~1.39eV) than that (1.425 eV) of ZB GaAs,[7] confirming the presence of type II band alignment at room temperature. Both spots near the base (Figure S8a) and top (Figure S8b) of the nanowire reveal that increasing the excitation fluence results in a blue shifting of the emission peaks. Further increasing the pump fluence to more than 50 μJ.cm^{-2} per pulse resulted in a broadening of the emission peak. This blue shifting and broadening of the emission can be attributed to band filling. At high pump fluences, a shoulder peak emerges at 1.52eV.

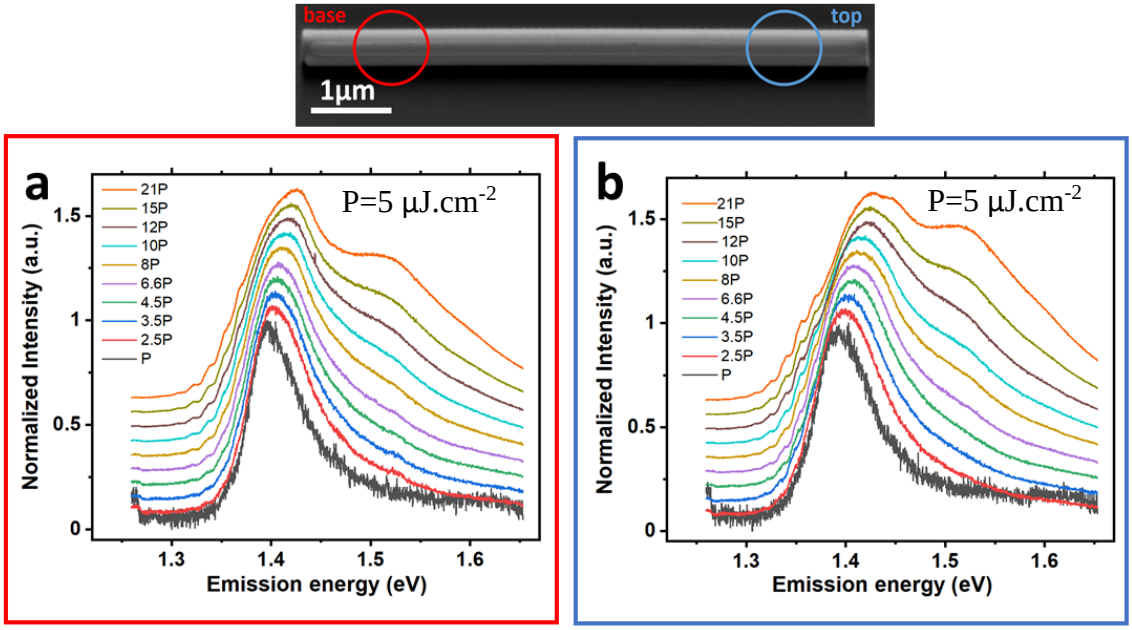

Figure S8. Power-dependent PL spectra from two spots located close to the base (a) and top (b) of a GaAs nanowire at room temperature.

4. Surface recombination velocity and lifetime of nanowires

4.1. Nanowires diameter for surface recombination velocity computation

The diameter of hexagonal nanowires grown via selected area epitaxy (SAE) is measured as the distance between the sidewalls.[19] However, for calculation of surface recombination velocity, the total surfaces on the sidewalls matters. Simplifying the hexagonal NW to a cylindrical one with the same surface area on the sidewalls follows:

$$6aL = 2\,\pi rL \qquad \text{(S1)}$$

where the L is the NW length, a is the hexagonal sidewall length and r is the radius of a cylindrical NW. Thus, a 460 nm hexagonal diameter is equivalent to a 507 nm cylindrical diameter (**Figure S9**).

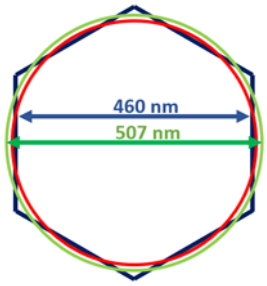

Figure S9. Hexagonal and equivalent cylindrical diameters for computing surface recombination velocity.

4.2. The PL lifetime and relationship between τ_{TDS} and n_{tdd}

The PL lifetime (τ_{PL}) a nanowire is determined by recombination at both surface states and twin defects. The PL lifetime τ_{PL} can thus be expressed as follows:

$$\frac{1}{\tau_{PL}} = \frac{1}{\tau_S} + \frac{1}{\tau_{TDS}} \qquad \text{(S2)}$$

where τ_S and τ_{TDS} are the lifetimes associated with recombination at surface states and twin defects, respectively. From Figure 3e in the main manuscript, the primary and secondary carrier lifetimes were assigned to surface recombination and recombination at twin defects, respectively.

To compute the surface recombination velocity (SRV) of the nanowires, the contributions of surface recombination and twin defects to the secondary and primary carrier lifetimes can be deconvoluted with the following equation:

$$\frac{1}{\tau_{PL}} = \frac{1}{\tau_{bulk_{ZB}}} + \frac{4S}{d} + c.{n_{tdd}}^{x} \qquad \text{(S3)}$$

where S=SRV, $\tau_{bulk_{ZB}}$, d, and n_{tdd} are the bulk ZB GaAs minority carrier lifetime, the NW diameter and the average twin defect densities, respectively. For the inverse relationship

between secondary lifetime and twin defect densities, x and c are the power and the proportionality constants, respectively. The first two terms in equation S3 are well established for contributions to the minority carrier lifetime.[20] The last term represents the lifetime component associated with the twin defect density and is proposed in this paper. This is formulated to account for the relationship between the local twin defect density and the secondary lifetime in the passivated GaAs, using a similar approach to that expressed for dislocation densities.[21] In passivated GaAs nanowires with a constant core diameter of 507 nm, the first two terms in equation S3 are constant, while twin defects density changes along the length. **Figure S10** shows the relationship between twin defect density and the inverse of secondary carrier lifetime. The red dotted line is the best fit to the experimental data with the extracted values of c = 0.185 ns^{-1} and x = 0.5.

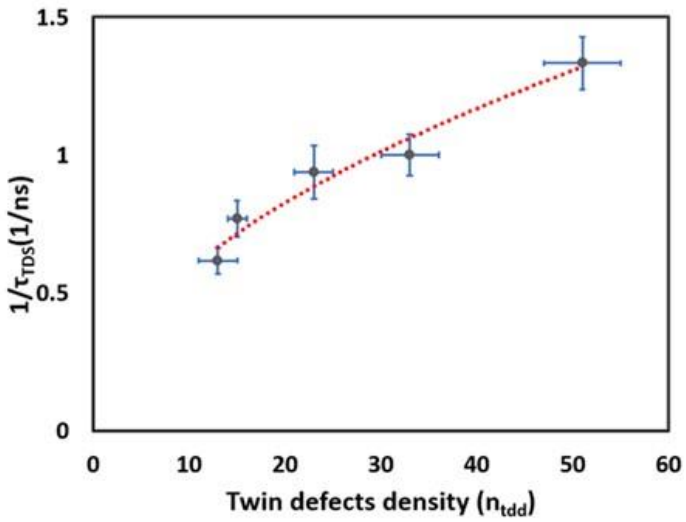

Figure S10. Secondary carrier lifetime as a function of twin defect density in GaAs/AlGaAs core/shell nanowire (the cylindrical diameter of GaAs core is 507 nm).

4.3. SRV at GaAs/AlGaAs interface

Using equation S2, PL lifetime (τ_{PL}) of 0.32±0.044 ns was computed along the GaAs/AlGaAs nanowire with the hexagonal diameter of 460 nm (cylindrical diameter of 507 nm), where n_{tdd} is less than 60 μm^{-1}. However, at the base of the passivated NWs where n_{tdd} is greater than 60 μm^{-1} a single exponential decay (red graph in Figure 3c) was observed. As a result, the

contributions from facets and twin defect sites are convoluted in equation: $\frac{1}{\tau_{PL}} = \frac{1}{\tau_{bulk,total}} + \frac{4S}{d}$, where $\tau_{bulk.total}$ represents both contribution of the recombination decay at ZB bulk GaAs structure and twin defects. The base of GaAs/AlGaAs nanowires with different diameters have twin defect density greater than 60 μm^{-1} which resulted in a single carrier lifetime. By using the equation $\frac{1}{\tau_{PL}} = \frac{1}{\tau_{bulk.total}} + \frac{4S}{d}$, SRV was extracted for the base. Figure **S11** shows the estimation of the SRV from the slope of the linear fit of inverse PL lifetimes vs inverse diameter for passivated GaAs (GaAs/AlGaAs) nanowires. We have also computed the SRV for the top of passivated nanowires. By using the equation $\frac{1}{\tau_{PL}} = \frac{1}{\tau_S} + \frac{1}{\tau_{TDS}} = \frac{1}{\tau_{bulk.total}} + \frac{4S}{d}$, SRV was extracted for the nanowires top, where twin defects density is lower than 20 μm^{-1}. In Figure S11, the constant slope at both the base and top of the nanowires indicates a constant SRV of 1.65 $\times 10^4$ cm/s along the nanowire length.

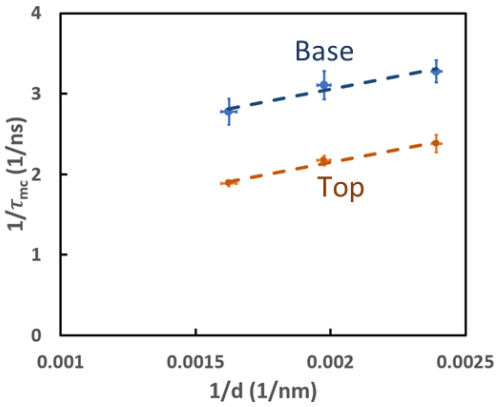

Figure S11. Minority carrier lifetime of GaAs/AlGaAs core/shell nanowires as a function of core diameter collected from the base and top of the nanowires.

4.4. SRV and τ_{bulk} of bare GaAs nanowires

Irrespective of diameter, the TRPL time decay reveals a single exponential decay, which does not change significantly within a 1 µm region in the middle of nanowires. Figure S12 shows the collected TRPL data of unpassivated nanowires with the diameters of 352 nm (red) and 735 nm (blue). The initial spike in the TRPL spectrum is due to the optical response time of our setup, which is round 80 ps.

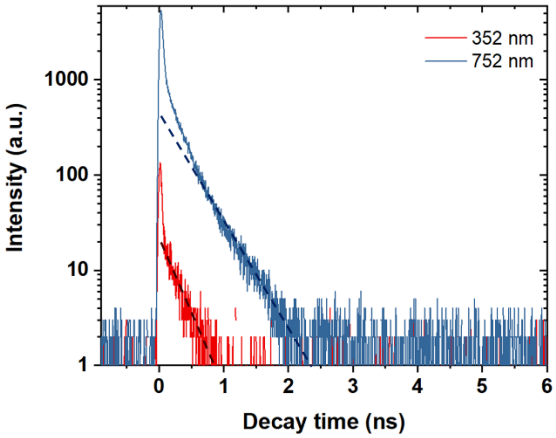

Figure S12. Time-resolved PL from the unpassivated GaAs nanowires with the diameter of 352 nm (red) and 735 nm (blue).

TEM results revealed that by increasing the NW diameter from 352 to 735 nm, the twin defect density (in the middle of the NWs) decreases from ~50 to ~30 μm^{-1}, respectively. In this diameter range , the average twin defect density n_{tdd} is about 40±10 μm^{-1}. The average lifetimes were calculated from the measurements of 8 NWs for each diameter. **Figure S13** is a linear plot of the reciprocal of the minority carrier lifetime with respect to the reciprocal of the nanowire diameter. Using equation (S3), we extract an SRV of 3.5 $\times 10^4$ cm/s from the gradient of the linear fit. The intercept gives us the value of $\frac{1}{\tau_{bulk}} + c40^x = 1.692\ ns^{-1}$.

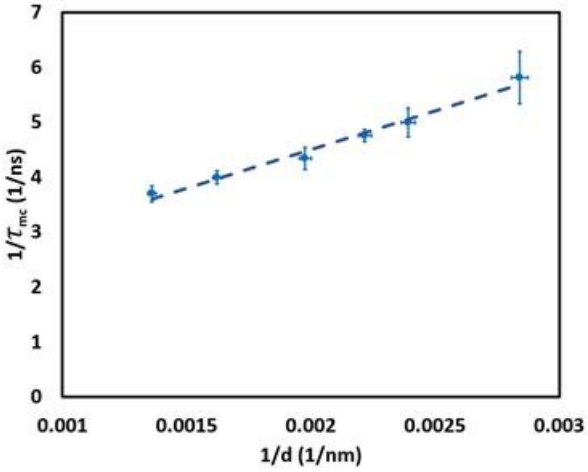

Figure S13. Minority carrier lifetime of GaAs nanowires as a function of nanowire diameter

4.5. Internal quantum efficiency

The internal quantum efficiency (IQE) of the NWs represents their optical quality and can be estimated by $\eta_i = \tau_{nr}/(\tau_{nr} + \tau_r)$, where τ_{nr} and τ_r are the non-radiative and radiative lifetimes, respectively. The quantum efficiency can be increased by either increasing the non-radiative lifetime through improvement of material quality and lowering SRV by a passivation layer or decreasing the radiative lifetime by impurity doping.[22–25] In this case the quantum efficiency is improved by increasing the non-radiative lifetime as a direct result of the lower SRV. At low excitation power at room-temperature, τ_{PL} is $\sim \tau_{nr}$ and the τ_r is computed from the estimated carrier density (N) and using $\tau_r = 1/BN$, where B is radiative recombination coefficient (2×10^{-10} $cm^3.s^{-1}$). The average generated carrier density (N) at different pump fluences in a NW can be estimated using:

$$N(cm^{-3}) = \frac{\eta_P . P_{ave}}{f_P \cdot {}^{hc}/_{\lambda_P} . V} \qquad \text{(S4)}$$

where P_{ave} (J/s), hc/λp (eV) and V (cm^3) are the pump power, the energy of pump photons and the volume of the NW, respectively. A femtosecond pulsed laser (f_p) with the frequency of 20.8 MHz was used as the excitation source. η_p is the pump efficiency which can be estimated from the absorption cross-section of the NW (σ_{abs} cm^2) over the area of excitation spot (A_p). In the passivated GaAs/AlGaAs core/shell NWs $\eta_p = f_{core}\sigma_{abs}/A_p$, where f_{core} is the fraction of power absorbed in the core relative to the total power absorbed in the NW. For GaAs/AlGaAs core/shell NWs, f_{core} of 0.65 was calculated from finite-difference time-domain (FDTD) simulations. Using 3D FDTD, absorption cross-sections (σ_{abs}) of 3×10^{-8} and 4.68×10^{-8} cm^2 were calculated for GaAs and GaAs/AlGaAs NWs, respectively. In this simulation, a cylindrical GaAs NW lying on a SiO_2 substrate was injected with the excitation source. Using the pump fluence relation, pump fluence= $\frac{P_{ave}}{f_P.A_P}$, and equation S4, carrier density can be estimated at different pump fluences:

$$N = \frac{f_{\,core} \cdot \sigma_{abs} \,.\, pump\ fluence}{hc/\lambda_P \,.V} \qquad \text{(S5)}$$

The pump fluence was computed at a large excitation beam, which covered the whole nanowire. More in details, the excitation spot size was enlarged using defocusing lens (f = 200 mm), so the focal spot size of < 1 µm with 60×(NA=0.7) objective lens was enlarged to the excitation spot size of 13.5 µm. Assuming τ_{nr} is independent of pump fluence, the quantum efficiency is calculated from τ_r and τ_{nr} as a function of excitation power density (**Figure S14**).

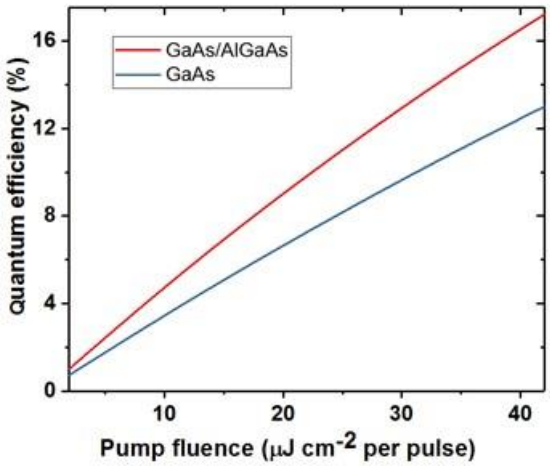

Figure S14. Internal quantum efficiency as a function of pump fluence for GaAs and GaAs/AlGaAs core/shell nanowires.

At a low pump fluence of 1 µJ.cm^{-2} per pulse, the non-radiative lifetime of 0.23±0.01 ns in GaAs and 0.32±0.044 ns in our AlGaAs passivated GaAs nanowire correspond to a quantum efficiency of ~ 0.37% and ~ 0.64% respectively.

The quantum efficiency of GaAs/AlGaAs nanowires reaches to ~30% just before the lasing threshold of 98 µJ cm^{-2} per pulse. This number increase to ~28% for bare GaAs before lasing at the pump fluence of 120 µJ cm^{-2} per pulse at low temperature.

4.6. Time-resolved PL decay of GaAs nanowires at 8 K

The PL lifetime of a GaAs nanowire was measured at pump fluences of 3 and 100 µJ.cm^{-2} per pulse. At the pump fluences of 100 µJ.cm^{-2} per pulse (below the lasing threshold of 120 µJ.cm^{-2} per pulse), the PL lifetime is 0.36±0.03 ns. This lifetime is shorter than the measured lifetime of 4±0.2 ns at lower pump fluence of 3 µJ.cm^{-2} per pulse. The reduction of lifetime from ~4 to

~0.36 ns might be related to local heating. With increasing temperature, the Fermi level moves closer to the valence band, emptying the trap energy levels in the minibands.[26,27]

The higher local temperature generated by the increasing pump power also increases the carrier density enabling more un-trapped carriers to reach the nanowire surface. As a result, the predominant recombination mechanism switches from being trap-driven to surface recombination-driven, leading to a significantly reduced carrier lifetime with excitation fluence.

5. Nanowires lasing

5.1. GaAs nanowire lasing at low temperature

The SAE grown NWs have a uniform hexagonal shape with a relatively flat broken end facet. This morphology provides a good optical cavity and gain medium. Lumerical MODE modelling was carried out to determine the guided Fabry-Perot cavity modes supported by our optically pumped GaAs nanowire laser. We modelled a cylindrical NW laying on a SiO_2 substrate, simplifying the hexagonal cross section to a circular one with the same cross-sectional area:

$$\frac{3\sqrt{3}a^2}{2} = \pi r^2 \qquad \text{(S6)}$$

where a and r are the hexagonal sidewall length and radius of the cylindrical NW, respectively. The waveguides and mode properties of these hexagonal and cylindrical NWs are similar.[28] Consequently, the relationship between a and r in equation S6 was used to compare the experimental results (hexagonal cross-section) and theoretical simulations (cylindrical cross-section). Notably, a 482 nm cylindrical diameter NW is equivalent to a 460 nm hexagonal diameter NW (**Figure S15**).

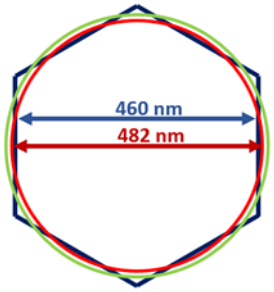

Figure S15. Hexagonal and equivalent cylindrical diameters to determine the gain cavity mode.

Using the refractive indices of GaAs (3.63) and SiO_2 (1.48), the supported lasing modes for different NW diameters were calculated at 870 nm, which is the room-temperature ZB GaAs band-edge emission. We calculated gain threshold g_{th} for all the supported guiding modes using:

$$\Gamma\, g_{th} = (1/L)\ln(1/R) \qquad \text{(S7)}$$

where Γ is the mode confinement factor, L is the length of the NW and R is the geometric mean reflectivities of both end facets. R and Γ were calculated for each supported guided mode using simulated field profiles and Lumerical modes simulations. **Figure S16** shows a plot of the gain thresholds for different cavity modes in a 7 μm long-cylindrical GaAs nanowire as a function of its diameter.

Based on our Lumerical MODE modelling, the lowest gain threshold of a GaAs nanowire with a cylindrical diameter of 482 nm is 228 cm^{-1} for the first transverse magnetic (TM01) mode. Increasing the excitation power from 228 cm^{-1} by 1.14 to 259 cm^{-1} results in additional lasing from hybrid electric (HE31a, HE31b) modes (Figure S16, green vertical line).

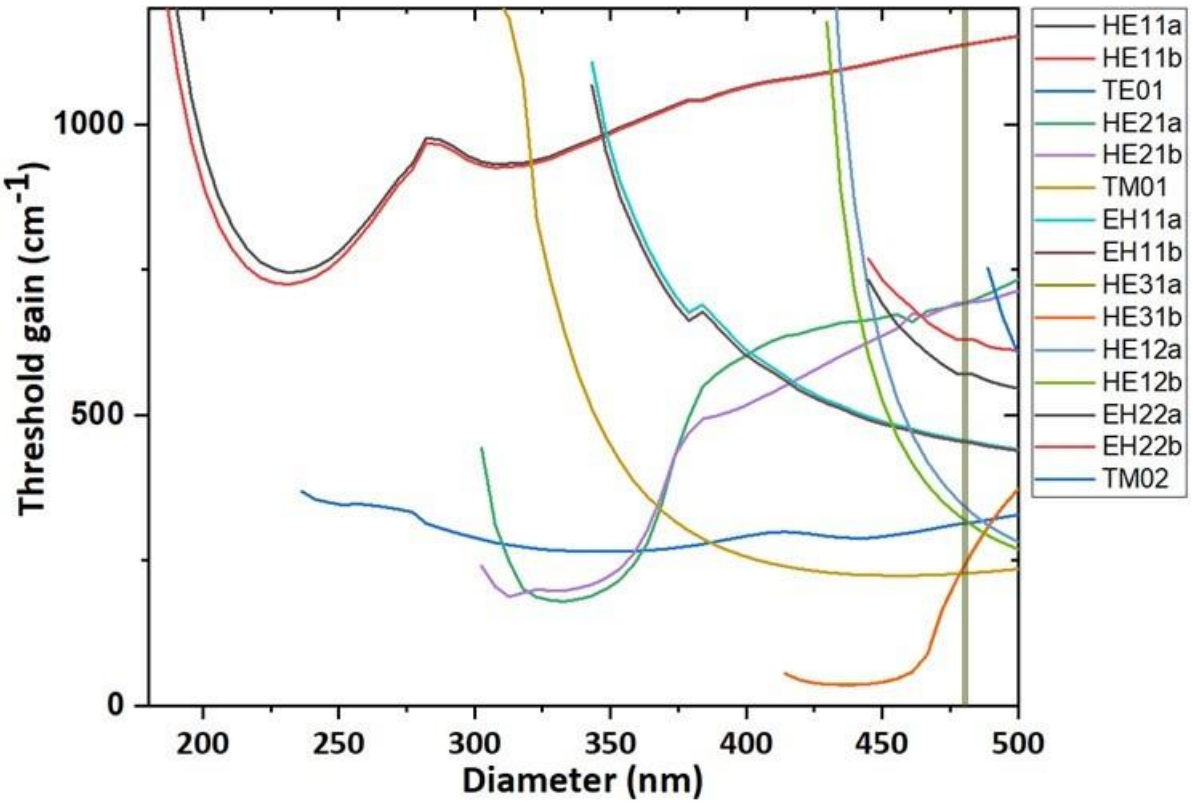

Figure S16. Modelled threshold gain of supported modes in unpassivated GaAs nanowires as a function of nanowire diameter. Green line shows for a nanowire with diameter of 482 nm, gain is lowest for the first transverse magnetic (TM01) mode.

It should be mentioned the reflectivity at the two ends of the nanowire was assumed to be from perfectly flat surfaces, while the nanowire was cleaved from the substrate with a glass needle and the edge of nanowire base was not flat (**Figure S17**). In addition, thermal effects due to poor thermal conductivity of SiO_2 and local heating with increasing pump fluence, were not taken into consideration in our simulation.

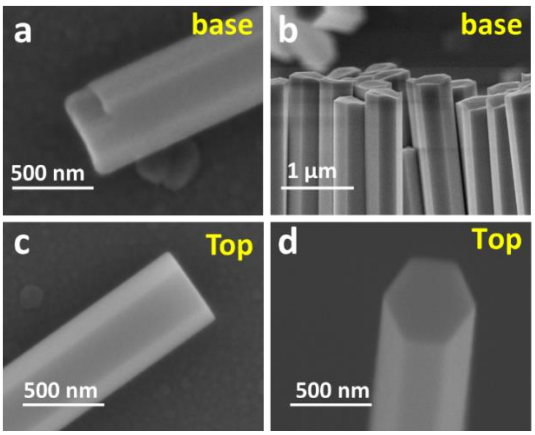

Figure S17. SEM images of the nanowires after picking them with a glass needle. (a) SEM images of a nanowire cleaved from its bases. (b) SEM images of the cleaved facets at the nanowires base. (c,d) SEM images of a nanowire with a flat top.

5.2. S curve fitting parameters for GaAs nanowires

Rate equations were used to estimate threshold gain (g_{th}), carrier density (N_{th}) and β factor of our GaAs NW lasers. Figure 4a reveals multimode lasing in the lasing spectra. Increasing the pump fluence to 120 μJ cm^{-2} per pulse activates two lasing modes at 848 and 852 nm. These lasing modes have relatively similar lasing thresholds, and their peak intensities grow rapidly with increasing pump fluence. Increasing the pump fluence activates additional modes, having higher lasing wavelengths of 858 and 862 nm. The presence of multiple lasing modes is best modelled with multimode rate equations, representing the various cavity modes observed. However, a single lasing mode rate equation was simply used to allow for numerical solutions to be computed. The rate equation and the validity of this simplification are both explained in more details in the rate equation analysis presented in the GaAs/AlGaAs NW section below.

The rate equation was used to fit the experimental data with a lasing threshold of 120 μJ cm^{-2} per pulse and an average gain peak position of 850 nm. This lasing threshold leads to a carrier density of 8.8×10^{18} cm^{-3}, which corresponds to a lasing temperature of 420 K at the gain peak position of 850 nm. The best fit for the simulated rate equation to the experimental data yields a threshold gain of g_{th} = 1600 cm^{-1} and a spontaneous emission factor of $\beta = 0.03$.

5.3. GaAs/AlGaAs nanowire lasing at room temperature

Using equation S6, the threshold gain (g_{th}), the mode confinement factor (Γ) and the geometric mean of both end facet reflectivities (R) were both calculated for a constant AlGaAs shell thickness of 27 nm and variable core diameters. **Figure S18** is a plot of the gain thresholds of the GaAs/AlGaAs core-shell NW as a function of NW diameter. By considering the GaAs cylindrical core diameter of 482 nm with an AlGaAs shell thickness of 27 nm, the overall cylindrical diameter of the passivated nanowire is 536 nm. For a NW with a diameter of 536 nm, the gain is the lowest (273 cm^{-1}) for the TM01 mode. While our SAE GaAs/AlGaAs

nanowire lasers have a larger diameter and a longer length than the VLS nanowire lasers,[25] they lase from the same TM01 mode.

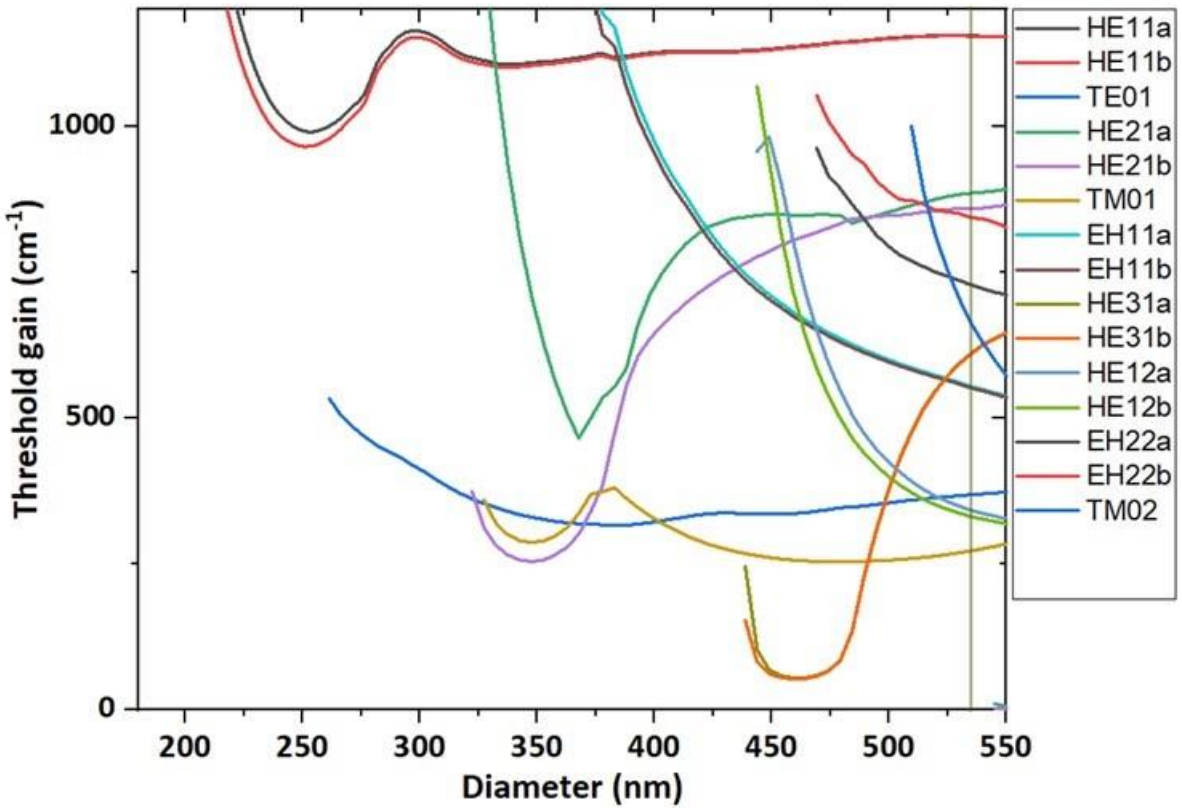

Figure S18. Modelled threshold gain of supported modes in passivated GaAs nanowires as a function of nanowire diameter. In a nanowire with the diameter of 536 nm, gain is lowest for the first transverse magnetic (TM01) mode.

5.4. Rate equation analysis for GaAs/AlGaAs nanowires

Rate equation analysis was used to estimate threshold gain (g_{th}), carrier density (N_{th}) and β factor of our GaAs/AlGaAs core/shell NW laser. Figure 5a shows two lasing modes in the lasing spectra. These two lasing modes with 3 nm difference in lasing wavelength have similar lasing threshold, while their relative intensity changes at different pump fluences. We assumed all the lasing parameters are the same for each of the two lasing modes and are equal to the average lasing parameters. With this assumption and not considering the interaction between lasing modes, the rate equation can be simplified to a single mode laser rate equation.

Rate equations for an optically pumped single mode laser can be written as:

$$\frac{dN}{dt} = \frac{\eta_p P}{\omega \hbar V} - AN - \frac{N}{\tau_{SP}} - CN^3 - v_g g S \qquad \text{(S8)}$$

$$\frac{dS}{dt} = \Gamma \upsilon_g (g - g_{th}) S_b + \Gamma \beta \frac{N}{\tau_{SP}} \quad \text{(S9)}$$

where N is the carrier density in the active region and S is the photon density in the lasing mode. $\frac{\eta_p P}{\omega \hbar V}$ is the generation rate while V, η_p, $\omega\hbar$ and P are the volume of NW core, the fraction of pump power absorbed in the core, the energy of pump photon and the optical pump power used, respectively.[25] Given the NW dimensions, η_p of 2% was estimated from the FDTD simulations. A, C, τ_{SP} and g are the non-radiative recombination coefficient, Auger recombination coefficient, spontaneous emission (radiative) lifetime and the material gain, respectively. In equation (S8) υ_g and Γ are the group velocity and confinement factor of lasing mode and β is the spontaneous emission factor. The material gain is a function of carrier density and follows the logarithmic model:

$$g(N) = g_0 \ln\left(\frac{N + N_s}{N_{tr} + N_s}\right) \quad \text{(S10)}$$

The parameters g_0, N_s and N_{tr} were determined from curve fitting: g_0 = 2100 cm^{-1}, Ns =-1.3×10^{18} cm^{-3}, $N_{tr} = 2.94\times10^{18}$ cm^{-3}. Note that the material gain was modelled at carrier density of 7.3×10^{18} cm^{-3}. Lasing temperature of 490 K was calculated at the given carrier density while the gain peak was located at 880 nm. The values of υ_g=5.947×10^9 cm/sec and Γ=1.3 were calculated for the TM01 mode at 880 nm. The analytical fit to the experimental data gives a threshold gain of 2800 cm^{-1} and β of 0.09. The β= 0.09 is higher than previously reported for GaAs/AlGaAs nanowire,[25] thus indicating that there is a higher fraction of spontaneous emission coupled into the lasing.

6. GaAs nanowires elemental composition

6.1. Electron Dispersive X-ray (EDX) Analysis

EDX analysis was conducted on GaAs nanowires to determine the elemental distribution and also to investigate the presence/absence of any unintentional doping. The aberration corrected

STEM (AC-STEM) instrument equipped with an electron dispersive X-ray (EDX) detector system which has a large solid angle of 0.9 srad and consequently a very high elemental sensitivity. We used ex-situ lift out method to place a single nanowire onto a bare ultrafine mesh copper grid (No carbon film). Our EDX analysis shows a homogenous distribution of Ga and As atoms without any detectable concentration of other elements throughout the nanowire length (Figure S19).

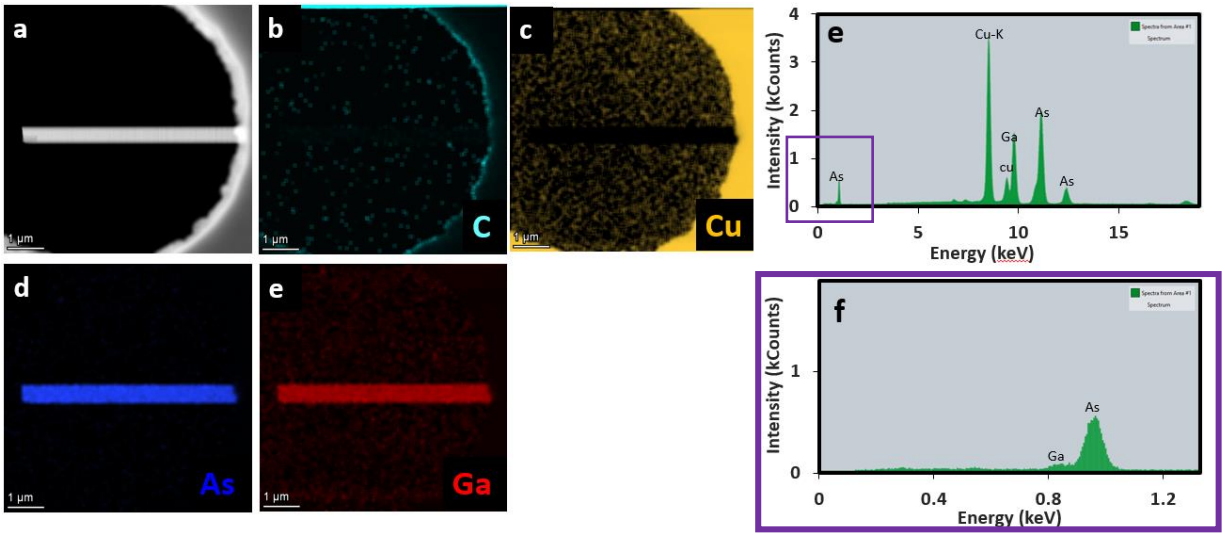

Figure S19. (a) STEM image of a GaAs nanowire and corresponding EDX mapping of (b) carbon, (c) copper, (d) arsine and (e) gallium. (d-e) show the uniformity of Ga and As composition along the length of the NW. (e) and (f) are EDX spectrum of the nanowire. Copper signal is from the carbon-free copper grid used for holding nanowires for STEM characterisation.

6.2. Atomic Probe Tomography (APT) Analysis

The APT analyses with ppm level elemental detection capacity showed a pure distribution of Ga and As atoms without any detectable concentration of other elements throughout the nanowire main axis and cross-section.

APT requires the field evaporation of atoms and was conducted on a needle-shaped sample with a tip diameter of ~ 100 nm, which is much smaller than the size of our nanowires (~500 nm in diameter). For this study, the GaAs nanowires were then sectioned by focused ion beam into 4 segments at different points along the axial direction, and each segment was attached onto a Mo post. FIB annular milling was used to thin down the post into a ~100 nm thick tip (tip along

the NW radial direction) ready for APT measurement. This offers the opportunity to investigate the impurities of the entire nanowire length (7 um) by sampling at 4 different sites. The detailed specimen preparation can be found in Figure S20(a-f) below.

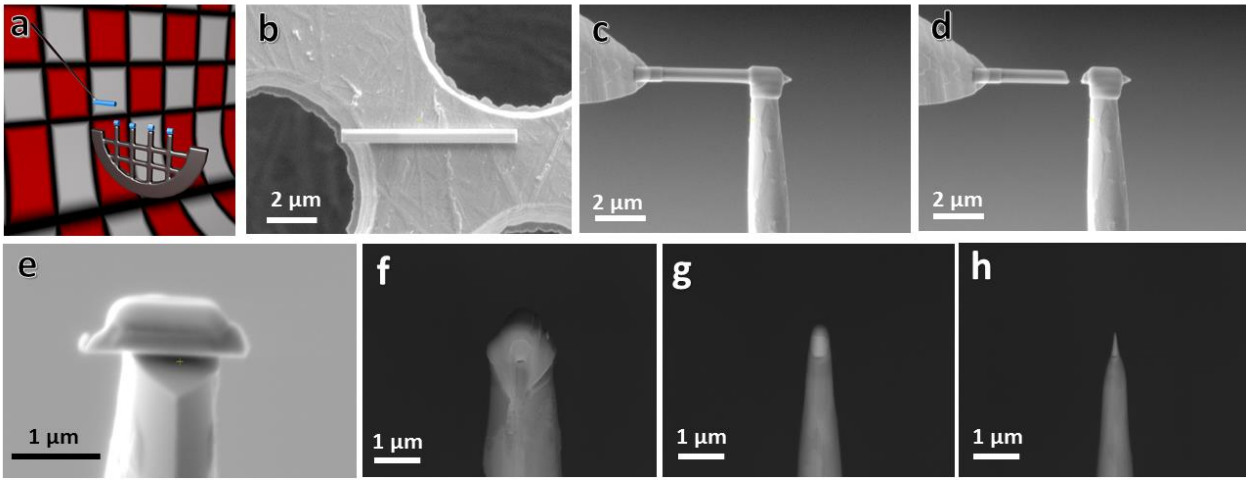

Figure S20. Preparation of four GaAs nanowires sections along the nanowire main axis for investigation of their radial composition by atom probe microscopy. a) Schematic representation of the GaAs sections along the nanowire. b) SEM images of a GaAs nanowire and (c-e) preparation of a section and (f-h) of the tip by FIB and milling.

The same section was prepared along the nanowire main axis for investigation of the axial composition by atom probe microscopy (Figure S21).

Figure S21 of the SI shows the analysis of a representative GaAs nanowire section by APT with z being along the axial direction of the nanowire. Arsine prefers to evaporate in the form of various cluster levels with different charge states. The typical mass spectrum shown in Figure S21.e shows that only Ga and As atoms were detected from the base to the top of the nanowire. More importantly, no signal from the impurities such as carbon and silicon were found in the detected region extracted from the base, middle and top regions of a single nanowire, respectively.

The APT analyses are consistent with EDX results and further confirm the non-detectable levels of dopants like C and Si.

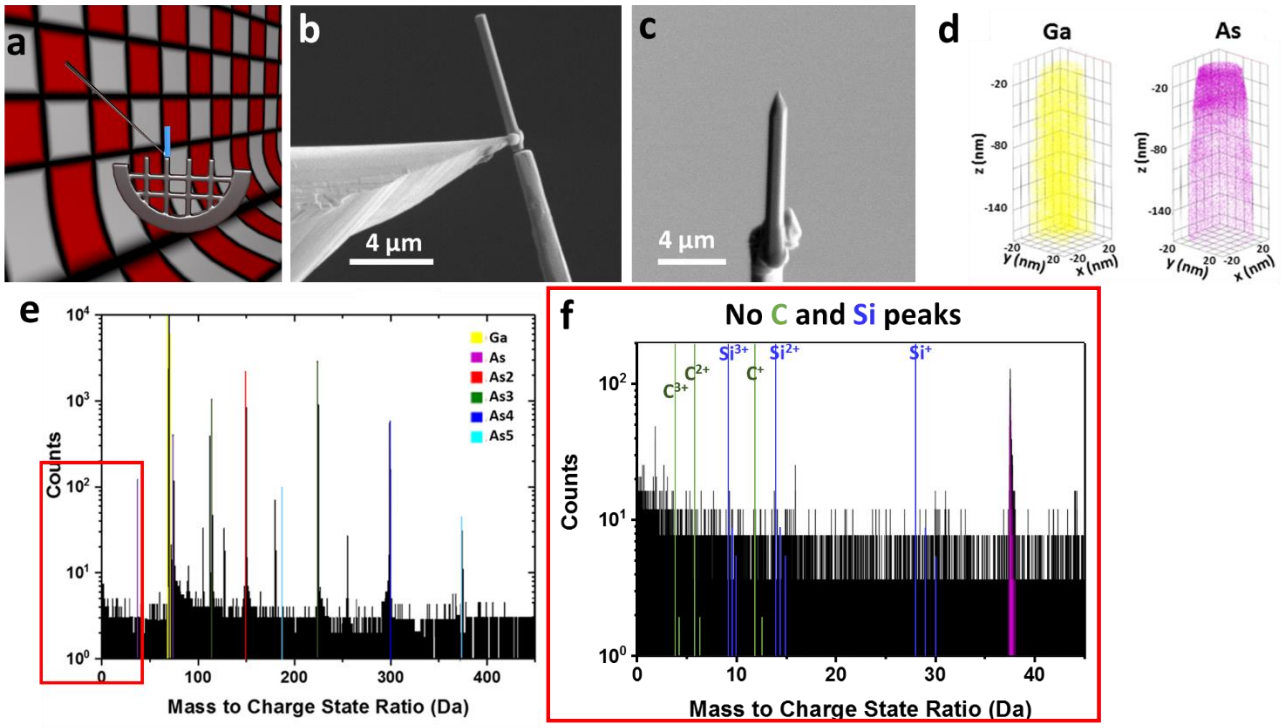

Figure S21. Schematic reparation of GaAs nanowires sections along the nanowire main axis for investigation of their axial composition by atom probe microscopy. (b,c) SEM images of nanowires preparation by FIB. (d) The distribution of Ga and As atoms along the axial direction of the nanowire. (e) Element count along the nanowire axial direction revealing only Ga and As atoms with different clustering ratios. (f) No detectable concentration of C and Si along the nanowire main axis.

1 P. Caroff, J. Bolinsson and J. Johansson, *IEEE J. Sel. Top. Quantum Electron.*, 2011, **17**, 829–846.

2 X. Yuan, L. Li, Z. Li, F. Wang, N. Wang, L. Fu, J. He, H. H. Tan and C. Jagadish, *Nanoscale*, 2019, **11**, 9207–9215.

3 A. Dobrovolsky, P. O. Å. Persson, S. Sukrittanon, Y. Kuang, C. W. Tu, W. M. Chen and I. A. Buyanova, *Nano Lett.*, 2015, **15**, 4052–4058.

4 B. Jiming, D. C. Bell, F. Capasso, J. B. Wagner, T. Mårtensson, J. Trägårdh and L. Samuelson, *Nano Lett.*, 2008, **8**, 836–841.

5 D. Spirkoska, J. Arbiol, A. Gustafsson, S. Conesa-Boj, F. Glas, I. Zardo, M. Heigoldt, M. H. Gass, A. L. Bleloch, S. Estrade, M. Kaniber, J. Rossler, F. Peiro, J. R. Morante, G. Abstreiter, L. Samuelson and A. Fontcuberta I Morral, *Phys. Rev. B - Condens. Matter Mater. Phys.*, 2009, **80**, 1–9.

6 U. Jahn, J. Lähnemann, C. Pfüller, O. Brandt, S. Breuer, B. Jenichen, M. Ramsteiner, L. Geelhaar and H. Riechert, *Phys. Rev. B - Condens. Matter Mater. Phys.*, 2012, **85**, 1–7.

7 M. Brewster, O. Schimek, S. Reich and S. Gradečak, *Phys. Rev. B - Condens. Matter Mater. Phys.*, 2009, **80**, 5–8.

8 A. Senichev, P. Corfdir, O. Brandt, M. Ramsteiner, S. Breuer, J. Schilling, L. Geelhaar and P. Werner, *Nano Res.*, 2018, **11**, 4708–4721.

9 M. De Luca, G. Lavenuta, A. Polimeni, S. Rubini, V. Grillo, F. Mura, A. Miriametro, M. Capizzi and F. Martelli, *Phys. Rev. B - Condens. Matter Mater. Phys.*, 2013, **87**, 1–8.

10 A. V. Senichev, V. G. Talalaev, I. V. Shtrom, H. Blumtritt, G. E. Cirlin, J. Schilling, C. Lienau and P. Werner, *ACS Photonics*, 2014, **1**, 1099–1106.

11 M. Heiss, S. Conesa-Boj, J. Ren, H. H. Tseng, A. Gali, A. Rudolph, E. Uccelli, F. Peiró, J. R. Morante, D. Schuh, E. Reiger, E. Kaxiras, J. Arbiol and A. Fontcuberta I Morral, *Phys. Rev. B - Condens. Matter Mater. Phys.*, 2011, **83**, 1–10.

12 B. Ketterer, M. Heiss, E. Uccelli, J. Arbiol and A. Fontcuberta I Morral, *ACS Nano*, 2011, **5**, 7585–7592.

13 N. Vainorius, S. Lehmann, D. Jacobsson, L. Samuelson, K. A. Dick and M. E. Pistol, *Nano Lett.*, 2015, **15**, 2652–2656.

14 J. Bolinsson, M. Ek, J. Trägårdh, K. Mergenthaler, D. Jacobsson, M. E. Pistol, L. Samuelson and A. Gustafsson, *Nano Res.*, 2014, **7**, 1–18.

15 H. J. Joyce, Q. Gao, H. H. Tan, C. Jagadish, Y. Kim, M. A. Fickenscher, S. Perera, T. B. Hoang, L. M. Smith, H. E. Jackson, J. M. Yarrison-Rice, X. Zhang and J. Zou, *Nano Lett.*, 2009, **9**, 695–701.

16 E. H. Bogardus and H. B. Bebb, *Phys. Rev.*, 1968, **176**, 993–1002.

17 H. J. Joyce, Q. Gao, H. H. Tan, C. Jagadish, Y. Kim, M. A. Fickenscher, S. Perera, T. B. Hoang, L. M. Smith, H. E. Jackson, J. M. Yarrison-Rice, X. Zhang and J. Zou, *Adv. Funct. Mater.*, 2008, **18**, 3794–3800.

18 M. J. Ludowise, *J. Appl. Phys.*, , DOI:10.1063/1.336296.

19 J. Noborisaka, J. Motohisa and T. Fukui, *Appl. Phys. Lett.*, 2005, **86**, 1–3.

20 H. J. Joyce, J. Wong-Leung, C. K. Yong, C. J. Docherty, S. Paiman, Q. Gao, H. H. Tan, C. Jagadish, J. Lloyd-Hughes, L. M. Herz and M. B. Johnston, *Nano Lett.*, 2012, **12**, 5325–5330.

21 M. Yamaguchi, A. Yamamoto and Y. Itoh, *J. Appl. Phys.*, 1986, **59**, 1751–1753.

22 T. Burgess, D. Saxena, S. Mokkapati, Z. Li, C. R. Hall, J. A. Davis, Y. Wang, L. M. Smith, L. Fu, P. Caroff, H. H. Tan and C. Jagadish, *Nat. Commun.*, 2016, **7**, 1–7.

23 B. Mayer, D. Rudolph, J. Schnell, S. Morkötter, J. Winnerl, J. Treu, K. Müller, G. Bracher, G. Abstreiter, G. Koblmüller and J. J. Finley, *Nat. Commun.*, 2013, **4**, 1–7.

24 B. Mayer, L. Janker, B. Loitsch, J. Treu, T. Kostenbader, S. Lichtmannecker, T. Reichert, S. Morkötter, M. Kaniber, G. Abstreiter, C. Gies, G. Koblmüller and J. J. Finley, *Nano Lett.*, 2016, **16**, 152–156.

25 D. Saxena, S. Mokkapati, P. Parkinson, N. Jiang, Q. Gao, H. H. Tan and C. Jagadish, *Nat. Photonics*, 2013, **7**, 963–968.

26 S. W. Johnston and R. K. Ahrenkiel, *AIP Conf. Proc.*, 1999, **462**, 505–510.

27 D. Rudolph, L. Schweickert, S. Morkötter, L. Hanschke, S. Hertenberger, M. Bichler, G. Koblmüller, G. Abstreiter and J. J. Finley, *New J. Phys.*, 2013, **15**, 113032.

28 A.-L. Henneghien, B. Gayral, Y. Désières and J.-M. Gérard, *J. Opt. Soc. Am. B*, 2009, **26**, 2396.